Mn local order in room temperature ferromagnetic Mn/ZnO multilayers

E Céspedes[1], **G R Castro**[1,2]**, F Jiménez-Villacorta**[1,2]**, A de Andrés**[1]
and C Prieto[1]

[1] Instituto de Ciencia de Materiales de Madrid, Consejo Superior de Investigaciones
Científicas, Cantoblanco, Madrid, 28049, Spain
[2] SpLine, Spanish CRG BM25 Beamline, European Synchrotron Radiation Facility, BP 220,
F-38043-Grenoble, France

Abstract
The local environment of Mn atoms in $(ZnO_{30 \text{ Å}}/Mn_t)_n$ multilayers (ML) has been studied by
means of x-ray absorption spectroscopy at the Mn K edge. A series of ML has been prepared by
sputtering with approximately constant total amount of Mn (300 Å) while the Mn layer
thickness (t) has been varied from 60 to 1 Å (modifying consequently the number of Mn–ZnO
interfaces) in order to study the Mn–Zn–O system. Variation of the Mn layer thickness (t) has
been directly associated with changes in the Mn oxidation states within the sample series.
Absorption spectroscopy results for films with $t \leqslant 15$ Å indicate mostly MnO_2 formation and
no signal of Mn in the ZnO lattice is found. Conversely, films with $t \geqslant 30$ Å present two
different Mn environments, that have been related to the coexistence of rocksalt and wurtzite
phases, formed by $Zn_{1-x}Mn_xO$ mixed solid solutions. The magnetic behaviour of samples is
correlated with structural properties. That correlation strongly points towards substitutional Mn
in the wurtzite phase as the origin of the observed ferromagnetism above room temperature.

1. Introduction

The Mn–Zn–O system has been widely studied in the last
few years due to its potential applications in magneto-
optoelectronic devices as a wide band gap diluted magnetic
semiconductor (DMS). Motivated by theoretical predictions
of room temperature ferromagnetism in $Mn_xZn_{1-x}O$ based on
the Zener model [1], efforts have been aimed at finding Curie
temperatures above room temperature (RT), which is essential
for building these devices. In the last few years, T_C higher
than RT has been achieved for Mn–Zn–O films prepared by
different methods [2]. However, paramagnetism [3], spin-
glass behaviour [4] and low temperature ferromagnetism [5]
have also been reported for apparently similar kinds of
samples. These differences, which contribute to stimulating
the debate on the actual origin of ferromagnetism in this
system, have currently promoted the development of detailed
and thorough structural characterizations of these complex
materials. X-ray absorption spectroscopy (XAS) is a powerful
tool for studying the local environment of a selected atom;
in particular the short range order around Mn in the Mn–
ZnO system has been lately studied using x-ray absorption
near-edge structure (XANES) and extended x-ray absorption

fine structure (EXAFS) spectroscopies. These experiments
have been used to show that Mn substitutes for Zn in the
ZnO wurtzite phase for instance in Mn-doped epitaxial ZnO
thin films [6], and in polycrystalline sintered samples for Mn
concentrations up to 5 at.% [7]. Additionally, high pressure
experiments have been carried out to probe Mn substituting
for Zn in the wurtzite phase and also in the rocksalt phase
after applying more than 8 GPa [8]. The magnetic behaviour
has been recently correlated with the Mn lattice position in
MBE prepared Mn–Zn–O films [9] where ferromagnetism is
observed at low temperatures and which might be originating
from substitutional Mn^{2+} in the wurtzite ZnO lattice. Lately,
Guo *et al* [10] have reported observations of room temperature
ferromagnetism in a 2.2 at.% Mn-doped ZnO thin film
deposited on fused quartz substrate by pulsed laser deposition,
and EXAFS study indicates that Mn^{2+} replaces the Zn site in
wurtzite.

On the other hand, high temperature ferromagnetism in
Mn–Zn–O system has been also achieved for a metastable
$Mn_{2-x}Zn_xO_{3-\delta}$ phase [11] developed by Zn diffusion into
Mn_2O_3 and several authors have recently reported Zn diffusion
into Mn oxide grains to explain the existence of room
temperature ferromagnetism [12, 13] that would have an

extrinsic origin, due to secondary phases [14]. In these cases, inter-diffusion between Mn and Zn oxides has been proposed to explain the appearance of ferromagnetism in this system, which is still a very intriguing point in this field.

Following these reported works, it is clear that Mn–ZnO interfaces are of huge interest in the study of Mn–Zn–O systems. For this reason, we have prepared a set of Mn/ZnO multilayers that, having approximately constant whole Mn amount, provide different numbers and thicknesses of Mn layers (and consequently, different numbers of Mn–ZnO interfaces) allowing one to study the reactivity between manganese and zinc oxides. In this paper, we report a Mn local order characterization obtained using EXAFS for Mn/ZnO multilayers and its influence on the observed magnetic behaviour.

2. Experimental details

Mn/ZnO multilayers (ML) were prepared by sequential DC sputtering on Si(100) substrates at room temperature. The base pressure provided by the vacuum system was in the 10^{-7} mbar range. ZnO layers were deposited by reactive sputtering from a pure Zn target (99.9%) using a O_2/Ar mixture gas (43% O_2 rich) at a working pressure of 5.4×10^{-3} mbar. Mn layers were grown from a Mn target (99.95%) at 5.0×10^{-3} mbar pressure of pure Ar. Pre-sputtering was performed before the multilayer growth and also between two consecutive layers. Deposition rates were about 0.07 nm s^{-1} for Mn and 0.05 nm s^{-1} for ZnO.

Following this procedure, a series of Mn/ZnO ML, labelled as $(ZnO_{30\,Å}/Mn_t)_n$, were prepared, maintaining the ZnO layer nominal thickness constant (30 Å) for every sample and changing the Mn layer nominal thickness (t) from 60 to 1 Å. A last additional 30 Å ZnO layer was deposited onto every sample.

XAS experiments were carried out at the BM25 beamline (SpLine) of the European Synchrotron Radiation Facility (ESRF), with a storage ring energy of 6 GeV and an average current of 200 mA. A Si(111) double-crystal pseudo-channel-cut monochromator was used for energy selection and the sample was vertically shifted while the spectrum was collected. The incident beam was monitored by means of an ion chamber filled with a mixture of N_2 and He, and the Mn and Zn Kα line fluorescence yield was collected using a Si(Li) detector, from e2v Scientific Instruments. The monochromator was detuned up to 30% for those energy ranges to reject components of higher harmonics. Several spectra were collected in order to improve the statistics and to have a good signal to noise ratio. Fluorescence spectra were obtained at room temperature under a geometry where the detector forms an angle of 90° with respect to the incoming beam. The energy calibration was monitored using Mn and Zn foils. Measurements of the Zn K edge were achieved by adding a Cr filter (6 μm foil) between the sample and detector and a smaller angle collection by increasing the sample–detector distance, in order to avoid saturation.

Rutherford backscattering spectroscopy (RBS) experiments were carried out at the Centro Nacional de Aceleradores at Sevilla with He^{2+} incident ions of 2 and 8 MeV. The beam
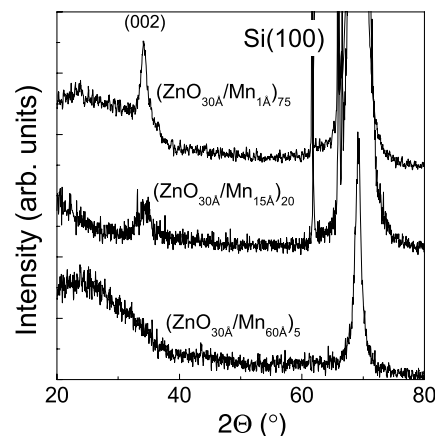

Figure 1. X-ray diffractograms of several representative samples.

diameter was about 1 mm and the dispersion angle was 165°. Details of the data analysis were given elsewhere [19].

X-ray diffraction (XRD) characterization measurements were carried out with a Bruker D8 x-ray diffractometer by using the Kα radiation line of Cu. Magnetic measurements were performed by means of a SQUID magnetometer (MPMS-5S from Quantum Design).

3. Results and discussion

As a first characterization approach, diffraction measurements on the sample series were carried out using a standard laboratory x-ray diffractometer. XRD spectra from several samples are shown in figure 1. The (002) peak corresponding to the ZnO wurtzite–hexagonal crystal structure can be clearly observed for samples with high enough ZnO content (being the samples with big enough number of layers, as the ZnO layer thickness is constant along the series); conversely, this peak is not observed for samples with few ZnO layers (as $(ZnO_{30\,Å}/Mn_{60\,Å})_5$ and $(ZnO_{30\,Å}/Mn_{30\,Å})_{10}$) most likely due to the small ZnO amount. No additional information on other Mn-containing phases can be extracted from XRD.

The magnetic behaviour of the ML series is shown in figure 2. Magnetization values have been normalized to the total amount of Mn in each sample, that was obtained from Rutherford backscattering spectroscopy experiments. Figure 2(a) gives the temperature dependence of the magnetization for some representative samples, showing a correlation between magnetic behaviour and the Mn layer thickness (t); room temperature ferromagnetism is obtained for some of the ML samples. The highest magnetization values are found for the sample with $t = 60$ Å, which presents ferromagnetic behaviour persisting above room temperature. As t is reduced, the ferromagnetic component of the magnetization decreases, while the paramagnetic one increases. Finally, very thin Mn layer samples ($t < 15$ Å) exhibit paramagnetic-like behaviour. The inset shows the Curie–Weiss behaviour for the $t = 1$ Å sample, which implies a negative Curie temperature ($\theta \approx -68$ K), indicating that the dominant magnetic interactions between Mn atoms

Figure 3. Mn K edge XANES spectra of Mn/ZnO multilayers and metallic Mn foil. The inset shows the determination of Mn oxidation state; the straight line represents the linear fit of the references. Open circles correspond to $t = 60$, 7 and 1 Å samples (from left to right).
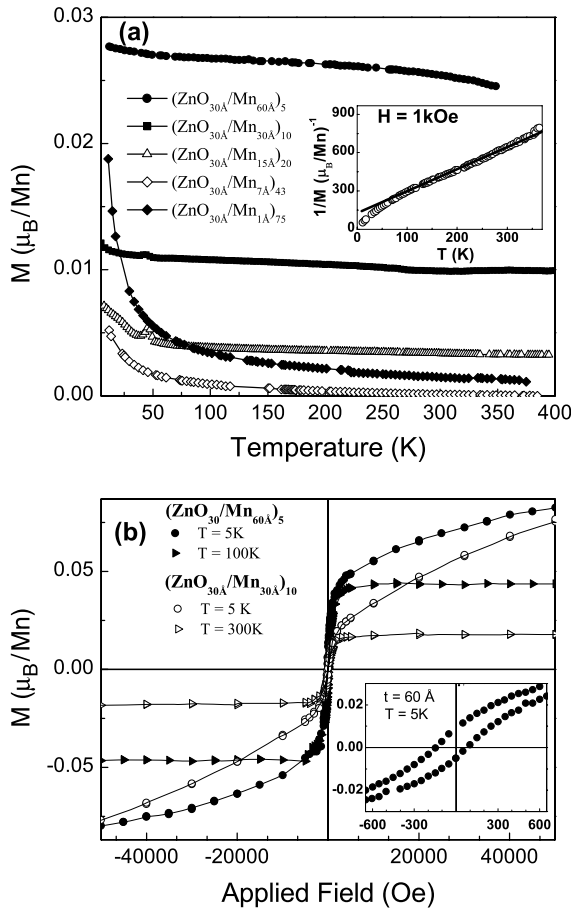

Figure 2. (a) Magnetization curves ($H = 1$ kOe) for several representative samples. The inset shows the inverse of magnetization versus temperature for the sample with $t = 1$ Å. The solid line corresponds to the linear fit from 100 to 350 K. (b) Hysteresis loops of $t = 60$, 30 Å samples at different temperatures. The inset shows the low field region of the hysteresis loop at 5 K ($t = 60$ Å sample).

are antiferromagnetic in nature, in agreement with some results previously reported for the Mn–ZnO system [15, 16]. Figure 2(b) shows hysteresis loops at several temperatures for two ferromagnetic samples. The sample with $t = 60$ Å exhibits about 0.05 μ_B per Mn atom, being the highest saturation magnetization among the studied samples, and a coercive field of approximately 80 Oe at 5 K.

Mn electronic states and the local structure of Mn/ZnO ML were investigated by means of x-ray absorption spectroscopy. Mn K edge XANES spectra of three representative samples and a Mn metal foil are displayed in figure 3. The Mn absorption K edge energy was calibrated by measuring a Mn foil and setting its E_0 value as in [17] to use the reported relative edge positions of the Mn compounds with different oxidation states. After edge jump normalization, direct comparisons can be made among the XANES spectra for all samples exhibiting a main edge energy shift, higher than 3.5 eV, from the thickest Mn layer sample ($t = 60$ Å) to the thinnest one ($t = 1$ Å), indicating an increase of the oxidation state as the Mn layer thickness decreases.

Edge energy values instead of pre-edge or white-line features are used to obtain the average Mn oxidation state,
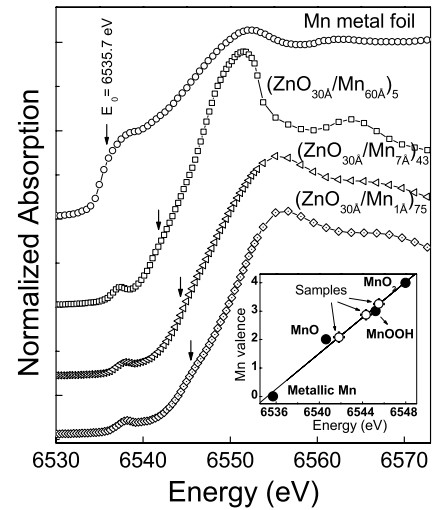
since for the data presented here this approach is more sensitive to Mn valence and least sensitive to structural effects. Taking into account the linear relationship between threshold energy and oxidation state for the reference compounds [17], the average oxidation state of Mn in these ML samples can be easily determined by measuring the threshold energy (inset of figure 3). It should be commented that for manganese oxides, the threshold energy values obtained from the maximum of the first derivative turns out to be affected by the splitting of the 1s–4p transition [18], which also affects the first-maximum position of the first derivative. For this reason, the threshold energy has been estimated in all cases as the energy corresponding to one third of the jump.

Results, summarized in table 1, reveal that Mn oxidation states range between Mn^{2+} and Mn^{4+}. ML with larger t in the series are related to Mn valence near to $+2$, while the ones with small t present oxidation states higher than $+3$. It is important to remark that under the experimental measuring conditions, the entire depth of the film is explored, contributing all Mn atoms from each sample to the Mn K edge XAS signal. This means that the obtained oxidation state value corresponds to the average of the actual distribution present in the whole film. The small slope obtained at the threshold for XANES spectra of ML indicates that Mn in the samples is not present in a pure oxidation state. The variation obtained for the Mn average oxidation state within the sample series has been explained taking into account the growth process [19]. ZnO layers are prepared by reactive sputtering from a pure Zn target using O$_2$/Ar mixture gas, which remains in the chamber for a while after finishing the ZnO growth. This turns the ZnO surface into an oxidizing environment for the first steps of the incoming Mn layer, that makes the first-deposited manganese very likely to be highly oxidized. Different interfaces are then expected at bottom or top of Mn layers, especially for Mn thickness that is sufficiently large, where the Mn can attain more reduced states.

In order to obtain precise information on the local environment (neighbours, coordination and bond length)

4

Table 1. Summary of XAS results corresponding to references and samples: XANES obtained Mn oxidation values and R, N and σ^2 EXAFS parameters (distance (R), number of neighbours (N) and the Debye–Waller factor, respectively). (The estimated error in the calculated Mn oxidation states is ± 0.2.)

Sample	Mn oxid. state	Mn–O			Mn–M			Zn–O			Zn–M		
		R (Å)	N	σ^2 (10^{-3} Å^2)	R (Å)	N	σ^2 (10^{-3} Å^2)	R (Å)	N	σ^2 (10^3 Å^2)	R (Å)	N	σ^2 (10^{-3} Å^2)
MnO	+2	2.22	6		3.14	12							
Mn$_3$O$_4$	+2	2.04	4										
	+3	1.93	4										
		2.28	2										
Mn$_2$O$_3$	+3	1.89–2.25	6										
β-MnO$_2$	+4	1.89	6		2.89	2							
					3.40	8							
ZnO								1.99	4		3.23	12	
Sputtered ZnO								1.97 ± 0.02	4	0.4 ± 0.5	3.18 ± 0.02	12	12 ± 1
(ZnO$_{30\,\text{Å}}$/Mn$_{60\,\text{Å}}$)$_5$	+2.1	2.03 ± 0.02	1.7	4.0 ± 0.5	3.11 ± 0.02	4.3	15 ± 1	1.98 ± 0.02	4.5	18 ± 0.5	3.12 ± 0.02	7.5	17 ± 1
		2.18 ± 0.02	1.6	5.0 ± 0.5	3.37 ± 0.02	4.0	18 ± 1				3.37 ± 0.02	4	6 ± 1
(ZnO$_{30\,\text{Å}}$/Mn$_{30\,\text{Å}}$)$_{10}$	+2.2	2.16 ± 0.02	5	8.0 ± 0.5	3.12 ± 0.02	7.3	11 ± 1						
					3.37 ± 0.02	2.7	9 ± 1						
(ZnO$_{30\,\text{Å}}$/Mn$_{15\,\text{Å}}$)$_{20}$	+2.6	1.94 ± 0.02	3.6	2.5 ± 0.5	2.86 ± 0.02	1.6	20 ± 1	2.05 ± 0.02	2.9	1.4 ± 0.5	3.14 ± 0.02	5	4.5 ± 1
(ZnO$_{30\,\text{Å}}$/Mn$_{7\,\text{Å}}$)$_{43}$	+2.9	1.92 ± 0.02	2.9	3.0 ± 0.5	2.91 ± 0.02	1.9	30 ± 1						
(ZnO$_{30\,\text{Å}}$/Mn$_{4\,\text{Å}}$)$_{75}$	+3.0	1.91 ± 0.02	4.5	2.5 ± 0.5	2.88 ± 0.02	1.0	50 ± 1						
(ZnO$_{30\,\text{Å}}$/Mn$_{1\,\text{Å}}$)$_{75}$	+3.3	1.93 ± 0.02	4.5	5.0 ± 0.5	2.91 ± 0.02	1.8	40 ± 1						

around Mn, EXAFS analysis was carried out at the Mn absorption K edge. EXAFS oscillations were obtained after removing the atomic background by a cubic spline polynomial fitting, and the EXAFS signal ($\chi(k)$) was found by normalizing the magnitude of the oscillations to the edge jump. The resulting data were transformed into a function of the photoelectron wavenumber, k.

The pseudo-radial distribution function around the absorber atoms has been calculated by Fourier transforming the k^2-weighted EXAFS signal ($k^2 \cdot \chi(k)$) multiplied previously by a Hanning window. To obtain neighbour distances and coordination numbers, the Fourier backtransform of the first and second peaks was fitted to the well-known expression [20]

$$\chi(k) = S_0^2 \sum_j \frac{N_j}{k R_j^2} e^{(-2k^2\sigma_j^2)} e^{(-2R_j/\lambda(k))} f_j(k)$$
$$\times \sin(2kR_j + \Phi_j(k)). \tag{1}$$

Equation (1) describes the EXAFS oscillations for a Gaussian distribution of N_j atoms at mean distances R_j around the absorbing atom, considering single-scattering and plane-wave approximations. S_0^2 is an intrinsic loss factor, N_j is the average coordination number for the Gaussian distribution of distances centred at the R_j value, σ_j is the Debye–Waller factor, and $\phi_j(k) = 2\delta(k) + \gamma_j(k)$ is the phase shift, $\delta(k)$ and $\gamma_j(k)$ being the central and backscattering atom phase shifts, respectively. $f_j(k)$ is the magnitude of the backscattering amplitude of the jth-neighbour atom, and λ is the mean free path of the photoelectron travelling from the absorbing atom to the backscatterer in the jth shell and the lifetime of the core hole.

Standard analysis was performed with the VIPER software [21]; for all the samples, FT were obtained over the same k^2-weighted interval (over a wavevector range from 2 to 10 Å^{-1}) by using amplitude and phase backscattering functions calculated using the FEFF6 code [22], where the scattering potentials are calculated in a standard way for atomic charge densities within the muffin-tin (MT) approximation. The potential also includes the Hedin–Lundqvist self-energy with the Quinn correction to account for low energy electron–hole losses. The conventional non-overlapping MT sphere approximation is used, since, for the EXAFS regime, the electron–atom scattering is dominated by the nearly spherical potential inside the muffin tin and has a low effect at these energies [23].

Figure 4 shows the Fourier transform (FT) magnitude of the EXAFS signal at the Mn K edge of the studied samples. Measurements on several manganese oxides, a standard Mn metal foil and a Mn thin film grown by sputtering were also made for comparison. It can be observed that all multilayer FT spectra present a first peak at ∼1.5 Å. This contribution is compatible with a Mn–O distance of about 2 Å, indicating the presence of oxidized Mn in the ML, in agreement with XANES studies. A noticeable difference between the FT of ML with thicker Mn layers ($t = 60, 30$ Å) and those for the other samples with thinner Mn layers can be observed in the graph. The positions and shapes of the FT peaks for samples with $t = 60, 30$ Å clearly differ from those corresponding
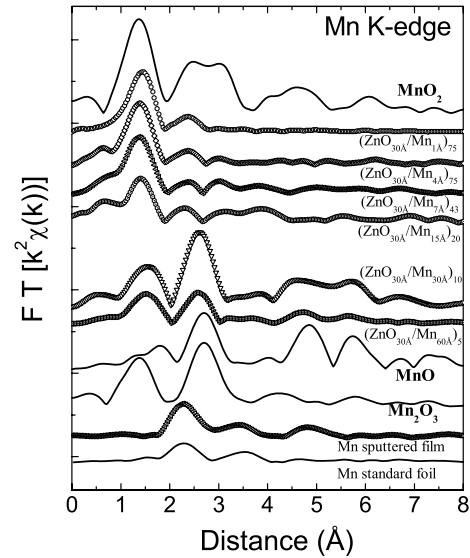

Figure 4. Experimental EXAFS Fourier transforms (FT) of the Mn/ZnO multilayer samples. The FT of manganese oxides, a Mn foil and a Mn sputtered thin film are shown for comparison.

to samples with $t \leqslant 15$ Å, all of them very similar, evidencing a difference in the structural properties between these two samples with thicker Mn layers and the others. From the magnetic measurements, a noticeable difference was also observed between the magnetic behaviours of these two samples and those of the others. ML with $t \geqslant 30$ Å exhibit ferromagnetic behaviour above room temperature, while in the case of samples with t below this value, the paramagnetic contribution increases and the magnitude of the magnetization becomes negligible. This suggests a direct relation between the ferromagnetic behaviour of these samples and the different Mn local structures that they present.

Standard EXAFS analysis provides the pairs and distances summarized in table 1, corresponding to the first and second coordination spheres. A comparison between experimental data and simulations for three representative samples can be observed in figure 5.

From the results obtained and in agreement with XANES data, shorter Mn–O distances are achieved from thinner Mn layer samples, evidencing higher Mn oxidation states in ML with $t \leqslant 15$ Å. For all these films the local environment around Mn is very similar. Mn–O and Mn–Mn distances obtained have values of 1.91–1.94 Å and 2.86–2.91 Å, respectively, which are very close to those in the β-MnO_2 structure [24]. Both the high Mn oxidation state and the pair distances ($R_{Mn-O} \sim 1.92$ Å and $R_{Mn-Mn} \sim 2.9$ Å) indicate mostly MnO_2 formation in samples with very thin Mn layers. The tendency of MnO_2 to be present in a non-stoichiometric state with Mn^{4+} vacancies, Mn^{3+} replacing Mn^{4+} cations and OH^- species replacing O^{2-} anions [25], can explain the oxidation states being slightly lower than +4 as well as the slight increase of atomic distances in the films.

It should be commented that the direct comparison between the FT corresponding to films with $t < 15$ Å and the MnO_2 reference does not show a match in magnitude for the
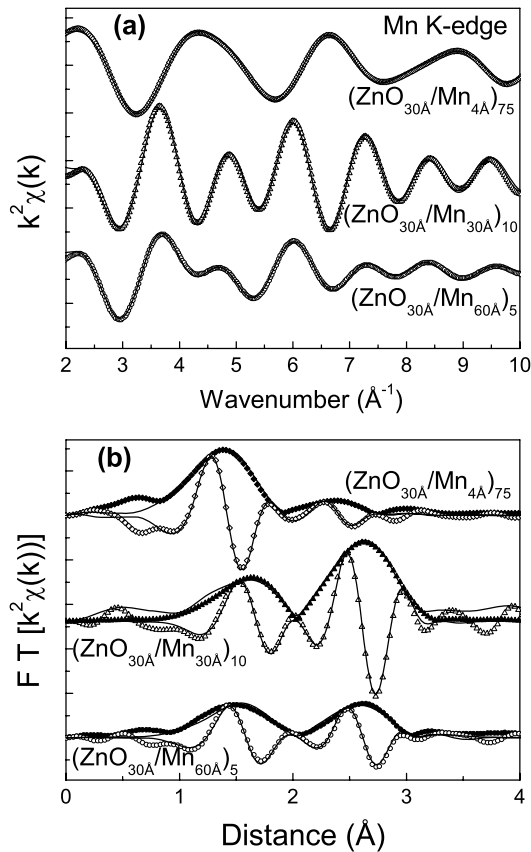
Figure 5. (a) k-space comparison between the experimental EXAFS signal (dots) and simulations (lines) at the Mn K edge for samples with $t = 60$, 30 and 4 Å. (b) Fourier transform of the (a) plotted signals; the modulus and imaginary parts have been presented for dual comparison with calculated contributions (lines).

second coordination sphere. The small magnitude observed for peaks corresponding to second coordination spheres is, undoubtedly, due to the very small MnO_2 grains obtained in the small Mn layers. This makes a significant reduction of the coordination number for coordination spheres beyond the first one [26], which provides an amorphous-like FT magnitude. For that reason, even if second FT peaks are not comparable in magnitude, the positions of the second peaks for samples with $t < 15$ Å match with MnO_2 as the fitted distances do (given in table 1).

Conversely and also in agreement with XANES results, in the case of samples with $t \geqslant 30$ Å, the obtained Mn–O distances ($R_{Mn-O} \sim 2.1$ Å) reveal an average Mn oxidation state near Mn^{2+} when comparing with the MnO reference, where $R_{Mn-O} \sim 2.2$ Å. Following a more refined EXAFS analysis, it is found that the $t = 30$ Å sample presents mostly a Mn–O contribution at $R_{Mn-O} = 2.16$ Å, while for the $t = 60$ Å sample two different Mn–O distances are provided by the fit, being 2.03 and 2.18 Å. Fits for both samples also show second-neighbour distances $R_{Mn-M} \sim 3.1$ Å and $R_{Mn-M} \sim 3.4$ Å, with M = Mn, Zn. It should be remarked that, for the analysed k-range interval, no significant differences were obtained when considering Mn or Zn as backscattering atoms. This means that, at least under the achieved experimental conditions, there

is no possibility of distinguishing between them (for this reason, only an R_{Mn-M} distance contribution, where M may be either Mn or Zn, is reported).

In the EXAFS analysis of these ML with larger values of t, not only Mn in ZnO wurtzite structure but also Mn in the rocksalt lattice should be considered. It is well known that wurtzite (W) is the stable form of ZnO, but under certain conditions, such as for high pressure, a rocksalt phase (RS) can be induced. When the relative Mn content in the $Zn_{1-x}Mn_xO$ solid solution is high, an enhanced stability of this rocksalt phase is expected since RS is the stable form of MnO. Results for the $t = 30$ Å sample are in good agreement with rocksalt structure: the obtained $R_{Mn-O} = 2.16$ Å is slightly smaller than the one corresponding to the MnO rocksalt (2.22 Å) but it is in full agreement with the distance (2.17 Å) from EXAFS for $Zn_{1-x}Mn_xO$ obtained for thin films by Pellicer-Porres *et al* [8]; in addition, second neighbours, found at $R_{Mn-M} = 3.11$ Å, match the geometrical condition between first and second distances in rocksalt structure ($\sqrt{2}$ ratio). Besides, there is a minor contribution, with $R_{Mn-M} = 3.37$ Å, that also appears for the $t = 60$ Å sample, and that will be explained below.

Results for the $t = 60$ Å sample indicate the same distance contributions as for the $t = 30$ Å sample corresponding to rocksalt structure, but in addition, EXAFS analysis shows here extra contributions with distances $R_{Mn-O} = 2.03$ Å and $R_{Mn-M} = 3.37$ Å that can be identified with the Mn substituting for Zn wurtzite phase [8, 27]. The obtained Mn–O distance is slightly higher than Zn–O in wurtzite structure, which is expected because the Mn^{2+} ionic radius is higher than the Zn^{2+} one. Moreover, this distance coincides again with the EXAFS obtained value for $Zn_{1-x}Mn_xO$ thin films [8] with wurtzite phase. Not much attention should be paid to the obtained coordination numbers for these samples (especially for the second shell); its high correlation with Debye–Waller factors, the small grain size effect as well as experimental difficulties due to self-absorption and short available k-space increase its own uncertainty.

In order to explain the whole series of samples, it should be noted that a small Mn^{4+} fraction deposited at the first growth stage of the Mn layer could be expected for all samples, since interfaces at the bottom of the Mn layer seem to be quite similar independently of the Mn layer thickness. For samples formed by the very thin Mn layers, no appreciable differences are expected at the bottom or top of the Mn layer, leading to the formation of a highly Mn oxidized phase throughout the whole layer. Conversely, in the case of samples with thicker Mn layers (nominally 30 and 60 Å) just the first-deposited Mn may be easily oxidized and become near the Mn^{4+} oxidized form. In this case, the thicker the Mn layer is, the less oxidized it becomes, implying noticeable differences between interfaces at the top and bottom of the Mn layer. Average Mn oxidation states of these two samples have been found to be $+2.1$ and $+2.2$ respectively, and although a small Mn^{4+} amount is expected at the bottom of the Mn layer, this fraction should be small comparing to the dominant phase, which is why it is not detectable using EXAFS.

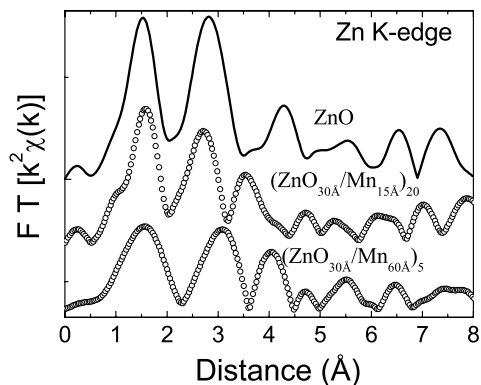Summarizing, EXAFS results can be understood in the following way: the Mn layer for the $t = 60$ and 30 Å samples

Figure 6. Fourier transforms (FT) of the Zn K edge EXAFS oscillation function $k^2\chi(k)$ for samples with $t = 60, 15$ Å and a 100 nm ZnO film.

is formed from $Zn_{1-x}Mn_xO$ oxide where the W and RS phases coexist. The formation of the RS phase in these ML samples is favoured by the high relative Mn contents in the samples, and also by the non-equilibrium growth conditions, which allows, for instance, stresses in the films. In principle, the relative contents of both phases should be related to the obtained coordination numbers, but the nanostructured character makes it impossible to deduce it from EXAFS data because of the finite size effect. Nevertheless, it is clear that the wurtzite phase content is higher for the $t = 60$ Å sample, as confirmed by the relationship between second-neighbour coordination numbers. It is worth noting that the low fraction of wurtzite phase in the $t = 30$ Å sample prevents resolving the two similar Mn–O distances.

The results show that two different Mn oxidation mechanisms have been observed in the preparation of this Mn/ZnO multilayer series. One of them is due to the oxygen excess at the surface of the later made ZnO layer that provides a full oxidation of the very close Mn atoms. Additionally, another oxidation mechanism has to be considered to explain the formation of Mn^{2+}. High reactivity of freshly deposited Mn layers may explain the inter-diffusion between Mn and ZnO observed by means of EXAFS and Mn oxidation. In this case, only the low oxidation state (Mn^{2+}) is reached, probably due to competition between Mn and Zn for sharing oxygen. In this way, it can be understood what in principle seems not to be consistent: that samples with the smallest Mn content do not show Mn diffusion into Zn oxide. The initial growth of the Mn layer leads mainly to the formation of MnO_2, meaning that neither Mn^{4+} diffusion into ZnO nor Zn diffusion into MnO_2 is expected, due to the big differences in their ionic radii [28].

Additional measurements were performed at the Zn K edges of samples. Figure 6 shows the Fourier transform magnitude for two ML samples ($t = 60, 15$ Å) and a ZnO sputtered film. The evaluation of the Zn environment in the $t = 15$ sample and ZnO sputtered film by comparing the corresponding FT shapes should be made just in its wide sense because the ZnO layer thicknesses in ML are only 30 Å, which allow both finite size effects that influences the TF magnitude and important strains such as those observed in figure 1, where a shift of the wurtzite ZnO peak is obtained
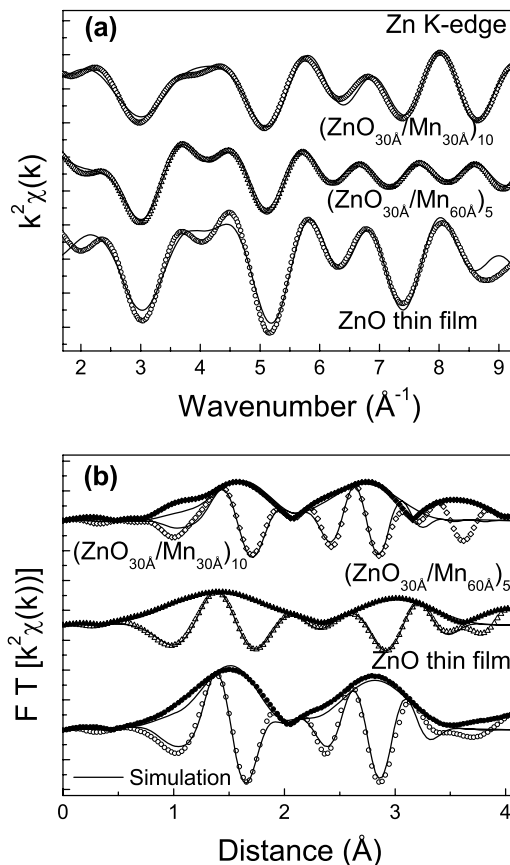

Figure 7. (a) k-space comparison between the experimental EXAFS signal (dots) and simulations (lines) at the Mn K edge for samples with $t = 60, 15$ and a 100 nm ZnO film. (b) Fourier transform of the (a) plotted signals; the modulus and imaginary parts have been presented for dual comparison with calculated contributions (lines).

for different samples. Standard EXAFS analysis provides pairs and distances summarized in table 1, corresponding to the first and second coordination spheres. Experimental data and simulations for the Fourier transform and Fourier backtransform of the EXAFS signal at the Zn K edge are shown in figure 7.

It can be observed that in the case of the $t = 60$ Å sample, the second peak of the FT magnitude reveals a second-neighbour contribution at higher atomic distances. Data analysis provides an additional Zn–M contribution at 3.37 Å. This result is fully in agreement with the Mn–M contribution found in the Mn K edge analysis of ML samples with $t > 15$ Å, supporting a model where layers containing Mn are composed of wurtzite and rocksalt phases, both of them formed from $Zn_{1-x}Mn_xO$ solid solutions.

Finally, in order to prove the validity of this model, the ML XANES spectra should be fitted as a linear combination of the XANES spectra corresponding to the Mn in each different phase, wurtzite and rocksalt, whose relative contents can be obtained from the fit.

Figure 8 shows the fits of the XANES spectra of samples with $t = 60$ and 30 Å. Pure phase spectra have been taken from experimental data in [8], where both phases have been obtained in the Mn–Zn–O system under the transformation induced by
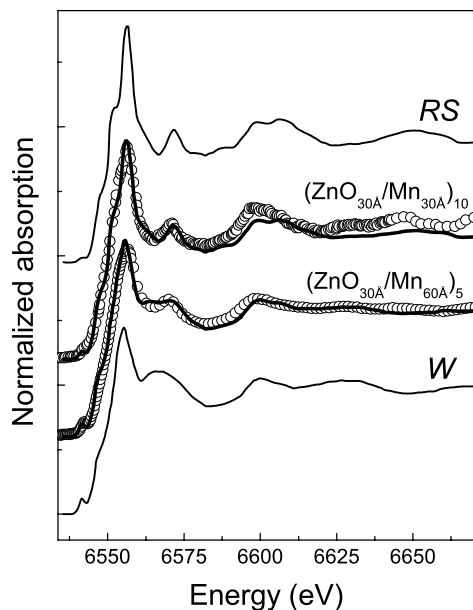
Figure 8. Experimental XANES spectra at the Mn K edge of $t = 60$, 30 Å multilayers (dots) and MnO in rocksalt (RS) and wurtzite (W) structures. Simulation curves (solid lines) of multilayer spectra obtained by linear combination of Mn in wurtzite (W) and rocksalt (RS) reference spectra are given for comparison.

hydrostatic pressure. The obtained relative contents of the two phases (RS = rocksalt; W = wurtzite phase) are [RS] = 25% and [W] = 75% for the $x = 60$ Å sample and [RS] = 70% and [W] = 30% for the $x = 30$ Å sample. If we take into consideration the magnetic properties of these two samples, the ratio between the saturation magnetization values of the samples, $M_S(t = 60$ Å$)/M_S(t = 30$ Å$)$, is approximately 2.5, the same value as for the relation between the wurtzite contents in the two samples, $[W]_{t=60 \text{ Å}}/[W]_{t=30 \text{ Å}}$, a fact that suggests that only Mn substituting for Zn in the wurtzite phase contributes to the observed ferromagnetism.

4. Conclusions

Room temperature ferromagnetism has been observed in Mn/ZnO multilayer samples with larger Mn thickness ($t \geqslant$ 30 Å) while Mn–Mn antiferromagnetic interaction dominates the magnetic behaviour of multilayers with thinner Mn layers ($t \leqslant 15$ Å).

Different electronic states within the sample series have been detected by means of XANES, being dependent on the Mn layer thickness (t). Mixed valence states are present in the films and the calculated average Mn oxidation state ranges from $+2.1$ to $+3.3$ as t is reduced.

Both XANES and EXAFS results indicate the formation of mostly β-MnO$_2$ in samples with very thin Mn layers ($t \leqslant$ 15 Å). Oxidation states lower than $+4$ are explained by the tendency of MnO$_2$ to be present in a non-stoichiometric form with cationic vacancies. No signal of Mn substitution into ZnO lattices is found in these ML.

For samples with $t \geqslant 30$ Å two different Mn environments are found by EXAFS studies at the Mn K edge and the

results suggest the coexistence of rocksalt and wurtzite phases. EXAFS analysis at the Zn K edge supports the formation of a $Zn_{1-x}Mn_xO$ mixed oxide composed of both phases, formed from solid solutions. Fits of the XANES with a linear combination of Mn spectra for wurtzite and rocksalt $Zn_{1-x}Mn_xO$ phases corroborate this hypothesis and provide the ratio between the two phases for the two ferromagnetic samples. Moreover, the same obtained value for the ratio between the magnetization saturations of the two samples strongly points towards Mn substituting for Zn in the wurtzite phase as being responsible for the observed ferromagnetism.

References

[1] Dietl T, Ohno H, Matsukura F, Cibert J and Ferrand D 2000 *Science* **287** 1019
[2] Chambers S A 2006 *Surf. Sci. Rep.* **61** 345
[3] Kim S S, Moon J H, Lee B, Song O S and Je J H 2004 *J. Appl. Phys.* **95** 454
[4] Fukumura T, Jin Z W, Kawasaki M, Shono T, Hasegawa T, Koshihara S and Koinuma H 2001 *Appl. Phys. Lett.* **78** 958
[5] Jung S W, An S, Yi G, Jung C U, Lee S and Cho S 2002 *Appl. Phys. Lett.* **80** 461
[6] Jin Z-W, Yoo Y-Z, Sekiguchi T, Chikyow T, Ofuchi H, Oshima M and Koinuma H 2003 *Appl. Phys. Lett.* **83** 39
[7] Kunisu M, Oba F, Ikeno H, Tanaka I and Yamamoto T 2005 *Appl. Phys. Lett.* **86** 121902
[8] Pellicer-Porres J, Segura A, Sánchez-Royo J F, Sans J A, Itié J P, Flank A M, Lagarde P and Polian A 2006 *Appl. Phys. Lett.* **89** 231904
[9] Xu W, Zhou Y, Zhang X, Chen D, Xie Y, Liu T, Yan W and Wei S 2007 *Solid State Commun.* **141** 374
[10] Guo J-H, Gupta A, Sharma P, Rao K V, Marcus M A, Dong C L, Guillen J M O, Butorin S M, Mattesini M, Glans P A, Smith K E, Chang C L and Ahuja R 2007 *J. Phys.: Condens. Matter* **19** 172202
[11] Kundaliya D C, Ogale S B, Lofland S E, Dhar S, Metting C J, Shinde S R, Ma Z, Varughese B, Ramanujachary K V, Salamanca-Riba L and Venkatesan T 2004 *Nat. Mater.* **3** 709
[12] García M A, Ruiz-González M L, Quesada A, Costa-Krämer J L, Fernández J F, Khatib S J, Wennberg A, Caballero A C, Martín-González M S, Villegas M, Briones F, González-Calbet J M and Hernando A 2005 *Phys. Rev. Lett.* **94** 217206
[13] Milivojevic D, Blanusa J, Spasojevic V, Kusigerski V and Babic-Stojic B 2007 *Solid State Commun.* **141** 641
[14] Blasco J, Bartolomé F, García L M and García J 2006 *J. Mater. Chem.* **16** 2282
[15] Gu Z, Lu M, Wang J, Wu D, Zhang S, Meng X, Zhu Y, Zhu S and Chen Y 2006 *Appl. Phys. Lett.* **88** 082111
[16] Lu J, Liang J K, Liu Q L, Liu F S, Zhang Y, Sun B J and Rao G H 2005 *J. Appl. Phys.* **97** 086106
[17] McKeown D A and Post J E 2001 *Am. Mineral.* **86** 701
[18] Croft M, Sills D, Greenblatt M, Lee C, Cheong S-W, Ramanujachary K V and Tran D 1997 *Phys. Rev.* B **55** 8726
[19] Céspedes E, Garcia-López J, García-Hernández M, De Andrés A and Prieto C 2007 *J. Appl. Phys.* **102** 033907

[20] Koninsberger D C and Prins R 1988 *X-Ray Absorption: Principles, Applications, Techniques of EXAFS, SEXAFS and XANES* (New York: Wiley)

[21] Klementiev K V 2001 *J. Phys. D: Appl. Phys.* **34** 209 VIPER for Windows, freeware: www.desy.de/~klmn/viper.html

[22] Zabinsky S I and Rehr J J 1995 *Phys. Rev.* B **52** 2995

[23] Rehr J J and Albers R C 2000 *Rev. Mod. Phys.* **72** 621

[24] Gilbert B, Frazer B H, Beltz A, Conrad P G, Nealson K H, Haskel D, Lang J C, Srajer G and De Stasio G 2003 *J. Phys. Chem.* A **107** 2839

[25] Figueroa S J A, Requejo F G, Lede E J, Lamaita L, Andrés Peluso M and Sambeth J E 2005 *Catal. Today* **107** 849

[26] Gay-Sanz N, Prieto C, Muñoz-Martín A, de Andrés A, Vázquez M and Yu S-C 1999 *J. Mater. Res.* **14** 3882–8

[27] Mokili B, Charreire Y, Cortes R and Lincot D 1996 *Thin Solid Films* **288** 21

[28] Peiteado M, Caballero A C and Makovec D 2007 *J. Solid State Chem.* **180** 2459